# Molecular Machines Stimulate Intercellular Calcium Waves and Cause Muscle Contraction

Jacob L. Beckham, Alexis R. van Venrooy, Soonyoung Kim, Gang Li, Bowen Li, Guillaume Duret, Dallin Arnold, Xuan Zhao, Ana L. Santos, Gautam Chaudhry, Jacob T. Robinson,* and James M. Tour*

J. L. Beckham, A. R. van Venrooy, G. Li, B. Li, D. Arnold, G. Chaudhry
Department of Chemistry, Rice University, 6100 Main Street MS 222, Houston, TX 77005 USA.

S. Kim, G. Duret, X. Zhao
Department of Electrical Engineering, Rice University, 6100 Main Street MS 222, Houston, TX 77005 USA.

A. L. Santos
Department of Chemistry, Rice University, 6100 Main Street, MS, 222, Houston, TX 77005 USA.
IdISBA - Fundación de Investigación Sanitaria de las Islas Baleares, Palma, Spain

Associate Professor J. T. Robinson
Department of Bioengineering, Department of Electrical Engineering, Rice University, 6500 Main Street, BRC 973, Houston, TX 77005 USA.
E-mail: jacob.t.robinson@rice.edu

Professor J. M. Tour
Department of Chemistry, Smalley-Curl Institute, NanoCarbon Center, Welch Institute for Advanced Materials, Department of Materials Science and Nanoengineering, Department of Computer Science, Rice University, 6100 Main Street MS 222, Houston, TX 77005 USA.
E-mail: tour@rice.edu

**Abstract**

Intercellular calcium waves (ICW) are complex signaling phenomena that control many essential biological activities, including smooth muscle contraction, vesicle secretion, gene expression, and changes in neuronal excitability. Accordingly, the remote stimulation of ICW may result in versatile new biomodulation and therapeutic strategies. Here, we demonstrate that light-activated molecular machines (MM), molecules that rotate and perform mechanical work on the molecular scale, can remotely stimulate ICW. Live-cell calcium tracking and pharmacological experiments reveal that MM-induced ICW are driven by the activation of inositol triphosphate ($IP_3$) mediated signaling pathways by unidirectional, fast-rotating MM. We then demonstrated that MM-induced ICW can be used to control muscle contraction *in vitro* in cardiomyocytes and animal behavior *in vivo* in *Hydra vulgaris*. Consequentially, this work demonstrates a new strategy for the direct control of cell signaling and downstream biological function using molecular-scale devices.

42 **Main**

43 Calcium signaling impacts nearly every process relevant to cellular life, and the ability of
44 calcium ions to alter protein shape and charge by reversible binding constitutes the most ubiquitous
45 signaling motif in receptor biology[1]. The localized nature of calcium signaling, as well as its ability
46 to activate downstream effector proteins, allows it to drive a vast array of biological activities. In
47 single cells, calcium directly controls cellular proliferation[2], gene expression[3,4], differentiation[5],
48 movement[6], and metabolism[7]. In organisms, calcium signals propagate through secondary
49 messengers to cause intercellular calcium waves (ICW) that coordinate concerted action in whole
50 tissues[8]. ICW play direct or indirect roles in processes ranging from muscle contraction[9],
51 potentiation of neuronal firing[10], blood vessel dilation[11], digestion[12], and breathing[13].
52 Dysfunctional calcium signaling contributes to disease states ranging from cancer to
53 cardiovascular disease and neurodegenerative disorders[14-15].

54 Due to the multiplexed nature of calcium signaling[16], the ability to remotely trigger ICW
55 with high spatiotemporal precision may permit access to numerous downstream signaling
56 pathways, offering a dynamic new strategy for the control of biological activity. Such advances
57 may also yield new therapeutic avenues for diseases characterized by calcium signaling
58 dysfunction. Currently, ICW are largely initiated experimentally by chemical methods[17] or by
59 applying mechanical stimuli using a micropipette attached to a microcontroller[2,8,18].

60 Here, we describe the generation of ICW *via* the nanomechanical action of a light-activated
61 molecular machine. Molecular machines (MM) are molecules that can be activated by external
62 stimuli, such as light, to perform mechanical work on the molecular scale[19]. Just as the mechanical
63 perturbation of a cell's outer membrane causes intracellular calcium responses, the application of
64 mechanical force *via* a fast, unidirectionally rotating MM elicits calcium release from the

65 endoplasmic reticulum (ER). Slow-rotating and non-unidirectional MM do not elicit calcium flux
66 under the same conditions, implicating a mechanism of action that depends on rapid, unidirectional
67 molecular rotation. Calcium release is attenuated by the inhibition of inositol triphosphate ($IP_3$)-
68 mediated signaling, suggesting the $IP_3$ signaling pathway as a primary driver of cellular responses.
69 Finally, we show that MM-induced ICW can be exploited to control downstream biological
70 processes, like muscle contraction, both *in vitro* and *in vivo*.
71

72 **Results and Discussion**

73 *Fast, Unidirectional MM Induce Calcium Waves*

74 MM employed in this study have overcrowded alkene motors based on the primary design
75 by Feringa *et al*[19]. Their typical structure consists of a rotor connected to a stator by an
76 atropisomeric alkene. When these MM are excited by incident photons, the rotor rotates
77 unidirectionally relative to the stator, undergoing two photoisomerization steps and two thermal
78 helix inversions before returning to the starting position (Fig. 1a). Overcrowded alkene motors
79 locomote in solution[20], drill through synthetic lipid bilayers and cell membranes[21], and have
80 previously been used to exert mechanical forces on individual cell-surface receptors *via* antibody
81 targeting[22]. Here, we study cellular responses to MM administered without the use of chemical
82 targeting or extracellular scaffolds, facilitating their use *in vivo*. The moiety "X" in Fig. 1a can be
83 interchanged to modulate MM rotation rate, which is determined by the favorability of the thermal
84 helix inversion step[23,24].

85 To investigate cellular responses to the actuation of MM, we employed live-cell calcium
86 tracking. HEK293 cells were treated with the fluorescent intracellular calcium indicator Fluo-4
87 and loaded with MM. The structures of the MM employed in this study are shown in Fig. 1b, and

88 the calcium responses of cells treated with fast-rotating MM **1** are shown in Fig. 1c. Stimulation
89 of a single MM **1**-treated cell with a 400 nm laser ($3.2\times10^2$ W $cm^{-2}$) increased Fluo-4 fluorescence
90 in the targeted cell, reflecting a spike in the intracellular calcium concentration similar to that
91 observed when cells are mechanically perturbed with a micropipette[8,18]. In the presence of the
92 vehicle only, no calcium responses were evoked by the same laser treatment (Supplementary Fig.
93 1). Calcium responses were observed to propagate to adjacent cells (Supplementary Fig. 2)
94 according to the degree of electrical connectivity between individual colonies. Similar responses
95 were observed when cells were treated with scavengers of reactive oxygen species (ROS,
96 Supplementary Fig. 3) and in experiments using X-Rhod-1 in place of Fluo-4 (Supplementary Fig.
97 4), suggesting that the observed responses do not depend on the production of ROS or fluorescence
98 resonant energy transfer between MM **1** and calcium tracking dyes.

99 Cellular responses to MM were repeatable (Supplementary Fig. 5), and their amplitude
100 could be controlled by the intensity of incident light (Supplementary Fig. 6). The strength of the
101 evoked response also determines the downstream effects of stimulation. At typical stimulation
102 irradiances ($3.2\times10^2$ W $cm^{-2}$ for 250 ms), cells recovered from stimulation and showed no signs of
103 apoptosis or necrosis (see Supplementary Fig. 7-8 and the accompanying discussion). Cells
104 stimulated at higher intensities ($6.4\times10^2$ W $cm^{-2}$ for 4 s) showed membrane blebbing and calcium
105 accumulation over a 30 min period, indicating cell death (Supplementary Fig. 9)[25]. Hence, MM-
106 induced ICW can be tuned between physiological, supraphysiological, and pathophysiological
107 response regimes by adjusting the stimulus intensity. Calcium responses induced by MM **1**
108 actuation were also observed in other cell lines, including neuroblast (N2A; Supplementary Fig.
109 10) and HeLa cells (Supplementary Fig. 11).

110 We investigated the calcium responses elicited by a library of MM consisting of two fast-
111 rotating motors (MM **1-2**) and two complementary motors (MM **3-4**) used to test the effects of
112 rotation speed and directionality (Fig. 1b). MM **1,** mimicking designs previously shown to kill
113 cancer cells and antibiotic-resistant bacteria[26-28], was synthesized with a six-membered ring stator
114 containing a central sulfur atom. MM **1** rotates unidirectionally at ~3 MHz. MM **2** and MM **3** are
115 chemically similar to MM **1** but rotate at different rates. MM **2**, which rotates at ~43 MHz, was
116 synthesized with a six-member ring stator with two methyl groups branching off the center carbon
117 atom[24]. MM **3**, a slow-rotating motor that rotates at ~0.1 Hz[24], was synthesized with a fluorene
118 stator. Finally, MM **4** is an analog to MM **1** that lacks a stereogenic center at the allylic methyl
119 site, which confers preference for unidirectional rotation. Without this stereogenic center, MM **4**
120 "flaps" bidirectionally and switches stochastically between photoisomerization states. All four of
121 these motors possess an appended aniline that shifts their absorption into the visible spectrum,
122 enabling their observation by visible-light microscopy and the activation of their rotation with
123 visible light[28]. These terminal amines are protonated at physiological pH, promoting their
124 interaction with the hydrophilic heads of lipid bilayers in cell or organelle membranes.

125 Fig. 1d shows the calcium responses of cells treated with each MM and light. MM **3** was
126 used at 3x concentration because of its lower extinction coefficient relative to the other MM
127 (Supplementary Fig. 12, Supplementary Table 1). Fast-rotating MM **1** and MM **2** elicited rapid
128 increases in intracellular calcium. MM **1** elicited high-amplitude transients that peak ~10-20 s after
129 stimulation and then decay over the next minute, whereas MM **2** elicited a more stable increase in
130 intracellular calcium that does not decay as quickly as MM **1**. The different calcium release kinetics
131 induced by MM **1** and MM **2** may be related to differences in their photoisomerization efficiency
132 (see the discussion in the Supplemental Information)[23]. Meanwhile, slow-rotating MM **3** elicited

133 no change in calcium activity upon irradiation, even at 3x the concentration and twice the stimulus
134 intensity used to activate MM **1** and MM **2** (Fig. 1d). MM **4**, the fast-rotating motor with no
135 preference for unidirectional rotation, elicited only small changes in calcium concentration. This
136 experiment provides evidence to link MM rotation speed and directionality to their evoked cell
137 signaling behavior.
138
139 *Mechanistic Study of MM-Induced ICW*
140 Next, we studied the biological mechanism behind MM-driven calcium signaling. Calcium
141 equilibrium in the cytosol is regulated by both export across the plasma membrane and uptake into
142 the ER *via* membrane ATPases (Fig. 2a)[1]. Consequentially, the cytosolic concentration of calcium
143 is typically low (~100 nM) compared to those found inside the ER or extracellular medium (~1.5
144 mM). Cytosolic calcium spikes commonly involve the entry of calcium from one of these two
145 locations. Fluorescence microscopy showed that MM internalize within cells and interact with
146 subcellular organelles, including mitochondria and the ER (Fig. 2b; Supplementary Figs. 13-14).
147 Since MM are distributed primarily within cells, we hypothesized that MM-induced calcium
148 responses arise from the release of calcium from intracellular stores. To test this hypothesis, we
149 depleted calcium stores inside and outside of HEK293 cells and blocked various plasma membrane
150 or ER calcium channels prior to stimulation (see Supplementary Table 2 for a complete list of the
151 manipulations employed in these experiments).
152 Cells treated with MM **1** and stimulated by light pulses in the absence of extracellular
153 calcium (Fig. 2c) showed no differences in response amplitude compared to a positive control in
154 calcium-containing medium. Similar results were observed when plasma membrane calcium
155 channels were blocked. Treatment of cells with ruthenium red (RR), a pharmacological inhibitor

156 of temperature-sensitive vanilloid transient receptor potential (TRP) channels[29], did not decrease
157 the magnitude of MM-induced calcium responses (Fig. 2d). Similarly, treatment of cells with $Gd^{3+}$,
158 which is commonly used to block the effects of mechanosensitive plasma membrane channels such
159 as Piezo1, Piezo2, and TRPC4[30], also did not affect the observed responses (Fig. 2e). In all, our
160 experiments show that plasma membrane TRP channels and extracellular calcium do not
161 appreciably contribute to MM-induced calcium responses.

162 On the other hand, cells treated with MM **1** and thapsigargin, a sarco-endoplasmic
163 reticulum calcium pump (SERCA) antagonist that depletes intracellular calcium[31], did not show
164 any measurable calcium flux upon light stimulation (Fig. 2f; $P = 0.00257 < 0.01$). This result
165 implies that MM-evoked calcium responses arise from the release of ER-bound calcium stores by
166 MM **1**.

167 Further mechanistic studies were conducted to determine how MM activation releases
168 calcium from the ER. The mammalian ER predominantly expresses two large tetrameric calcium
169 channels: $IP_3$ receptors ($IP_3Rs$) and ryanodine receptors (RyRs)[1,32]. In $IP_3$-mediated calcium
170 signaling, G-protein coupled receptors (commonly Gq/11 subtypes) expressed in the plasma
171 membrane activate phospholipase Cβ (PLCβ) and tyrosine kinase receptors activate PLCɣ to
172 cleave phosphatidylinositol 4,5-biphosphate into diacylglycerol and $IP_3$[32]. $IP_3$ can then diffuse to
173 the ER, where it binds to $IP_3R$ and causes calcium release. The activation of this network drives
174 such a wide array of cellular activities that it is often referred to as simply "calcium release" due
175 to its ubiquity in receptor biology[1]. RyRs are also expressed in many cell types and amplify
176 existing calcium signals through calcium-induced calcium release.

177 Treatment of cells with ryanodine (Ry; 100 μM) to block RyR signaling has no effect on
178 response amplitude (Fig. 2g) in HEK293 cells. However, treatment of cells with xestospongin C

179 (XeC; 25 μM), a known antagonist of $IP_3R$[33], significantly diminished the strength of cellular
180 responses to MM (Fig. 2h; $P = 0.0167 < 0.05$). Similar effects were observed when cells were
181 treated with the PLC antagonist U-73122 (U-73; 10 μM) as an alternate method of blocking $IP_3$
182 signaling (Fig. 2i; $P = 0.0281 < 0.05$). Furthermore, MM-induced responses were also inhibited
183 in cells treated with cytochalasin D (Cyto D; 2 μM), an inhibitor of F-actin polymerization that
184 disrupts PLC signaling by increasing the spatial distance between PLC and $IP_3R$ (Fig. 2j; $P =$
185 $0.01762 < 0.05$)[34]. These results implicate $IP_3$ signaling as a primary driver of MM-induced
186 calcium waves. The $IP_3$ pathway is known to contribute to mechanosensitive calcium currents[35]
187 and is also involved in the induction of ICW in response to mechanical stimulation with a
188 micropipette[2,18].
189
190 *MM Cause Muscle Contraction In Cardiomyocytes*
191 Next, we investigated whether MM-elicited ICW could be used to modulate calcium-
192 driven biological processes, such as the beating activity and contraction of cultured
193 cardiomyocytes. Fig. 3 shows the effects of MM stimulation on primary rat cardiomyocytes. MM
194 distribute to the sarcoplasmic reticulum (SR; Fig. 3a), where subsequent light activation triggers
195 localized calcium release (Fig. 3b, Supplementary Movie 1). MM-induced calcium release initially
196 leads to localized myocyte contraction at the site of stimulation (Fig. 3c, kymograph 1, top arrow)
197 likely due to the calcium-mediated activation of troponin and subsequent actin-myosin cross-
198 bridge formation[36]. Then, SR calcium release induces beating in quiescent cardiomyocytes and
199 accelerated beating in active cardiomyocytes (Fig. 3c, bottom arrow in kymograph 1 and arrow in
200 kymograph 2; Supplementary Movie 2).

201 We tracked the behavior of colonies of cardiomyocytes in contact with cells stimulated
202 with MM and light to determine whether we could use MM to drive biological behaviors
203 coordinated in networks of cells, such as contraction. Colonies of cardiomyocytes adjacent to
204 stimulated cells responded to stimulation by firing action potentials (APs) or participating in the
205 generated calcium wave (Fig. 3d; Supplementary Figs. 15-16). Activation of adjacent
206 cardiomyocytes in response to stimulation could be prevented by either inhibiting $IP_3$-mediated
207 calcium release in the stimulated cell (Fig. 3e) or by preventing the influx of calcium from outside
208 the cell during AP firing (Fig. 3f). Cells stimulated with MM **1** and light in calcium-containing
209 medium exhibited firing rates of 5.1 spikes $min^{-1}$ $cell^{-1}$, whereas cells stimulated with MM **1** and
210 light in the presence of PLC inhibitor (U-73; 10 μM) exhibited firing rates of ~0.8 spikes $min^{-1}$
211 $cell^{-1}$ ($P < 0.0001$ by a one-tailed Welch's t-test). Meanwhile, cells stimulated in the absence of
212 extracellular calcium did not exhibit any spiking activity, suggesting that the increased activity of
213 cardiomyocyte colonies in response to MM may be due to the action of voltage-gated ion channels
214 in the plasma membrane of myocytes. These ion channels are likely triggered by local
215 depolarization of the membrane induced by SR calcium release[37]. These experiments show that
216 biological behaviors coordinated in networks of cells, such as contraction, can be controlled by
217 intracellular MM-induced calcium wave generation.
218
219 *MM Control Behavior In Vivo*
220 Finally, using an *in vivo* model of muscle contraction, we sought to investigate whether
221 MM-induced ICW can control biological activity at the organism level. For this purpose, we chose
222 *Hydra vulgaris* as a model system. *Hydra* are radially symmetric, millimeter-sized freshwater
223 cnidarians containing tentacles, an oral region, and an aboral region connected by a long, tubular

224 body column. In the oral region, *Hydra* have a dome-shaped structure called a "hypostome"
225 surrounded by a ring of tentacles. At the other extremity, they have a foot called the "peduncle,"
226 which the animal uses to attach to substrates (Fig. 4a). *Hydra* were chosen as a model system
227 because of their small size, lack of chitin layer, excitable epitheliomuscular tissue, and simple
228 nervous system. In addition, *Hydra* exhibit spontaneous and stimulus-controlled contractions, both
229 driven by ICW[38], which can be directly visualized due to their transparent body. In our
230 experiments, we used *Hydra* lines genetically engineered to express the calcium indicator
231 GCaMP7b in their endothelial epitheliomuscular tissue (see *Methods*).

232 Prior to stimulation experiments, *Hydra* were loaded with MM by incubating with solutions
233 containing 24 μM of MM for 24 h (Fig. 4b). Distinct stimulation protocols were employed to cause
234 either local ICW or whole-body contraction (Fig. 4c). First, treatment of MM-loaded *Hydra* with
235 pulses of laser light administered to a small region of the body column (Protocol **I**) caused ICW
236 emanating from the site of stimulation (Fig. 4d; Supplementary Fig. 17; Supplementary Movies
237 3-4). Similar to ICW evoked *in vitro*, these ICW propagated throughout the *Hydra* body column
238 according to the degree of electrical connectivity of the stimulated cells. Distinct propagation
239 kinetics were observed when stimulating different regions of *Hydra* simultaneously
240 (Supplementary Movie 5). Second, we attempted to use MM activation to drive whole-body *Hydra*
241 contractions by administering laser stimuli to the oral region (Protocol **II**). We decided to target
242 the oral region because mechanical stimulation of this region has been shown to stimulate burst
243 contraction, likely *via* the sensory neurons that cluster in this region[39-41]. When laser stimuli were
244 delivered to the oral region of *Hydra* treated with fast-rotating MM **1** and **2** (Protocol **II**), they
245 exhibited contraction bursts associated with whole-body calcium waves (Supplementary Movie 6)
246 similar to those observed with macro-mechanical stimulation[42].

247 Fast-rotating MM were generally more successful in eliciting both regional ICW (Protocol
248 **I**) and whole-body contractions (Protocol **II**). Fig. 4e-i show responses from MM-treated *Hydra*
249 when stimulated *via* Protocol **I** to elicit regional ICW. Furthermore, Fig. 4j compares the response
250 rates of *Hydra* treated with each MM for exhibiting regional ICW. Fast-rotating MM, including
251 MM **1**, MM **2**, and even non-unidirectional fast motor MM **4**, consistently elicited robust regional
252 ICW upon stimulation of the body column (Protocol **I**). Occasional responses were also observed
253 from *Hydra* treated with slow-rotating MM **3**, but the response rate of these *Hydra* was not
254 significantly different from solvent-only controls (Fig. 4j). *Hydra* also demonstrated marked
255 differences in response kinetics depending on the type of MM employed. Fast, unidirectionally
256 rotating MM elicited appreciably quicker responses (12.76 s for MM **1** and 9.05 s for MM **2**) than
257 slow or non-unidirectionally rotating MM (15.46 s for MM **3** and 16.6 s for MM **4**; Fig. 4k).
258 Similar trends were observed for whole-body contractile response rates across *Hydra*
259 treated with different MM and light conditions (see *Methods* for a detailed description of the
260 response rate calculation). Fig. 4l-m show a representative whole-body contraction and GCaMP7b
261 fluorescence trace from a typical experiment using MM **2** and stimulation using Protocol **II**. In
262 these experiments, the fastest-rotating MM, MM **2**, was most successful at inducing *Hydra*
263 contraction, demonstrating a response rate of 86% (Fig. 4n). This fast-rotating MM elicited
264 contraction of *Hydra* at a higher rate than light alone ($P < 0.00001$) or slower-rotating MM **3** ($P <$
265 $0.00001$) by Fisher's Exact Test. MM **1** also elicited contraction at a significantly higher rate than
266 light alone ($P = 0.0199 < 0.05$), while the slow-rotating MM **3** ($P = 0.5325 > 0.05$) did not elicit
267 contraction at a significantly higher rate than light alone. Interestingly, MM **4**, which rotates
268 quickly but non-unidirectionally, elicited *Hydra* contraction with a response rate of 65% and was
269 significantly ($P = 0.0439 < 0.05$) more effective than light alone. MM **4** also elicited regional ICW

270 in *Hydra* despite causing only weak responses *in vitro*. These results imply that even the smaller
271 responses elicited by MM **4** *in vitro* can be amplified *in vivo* across networks of cells.
272 Consequentially, rotor speed is a better indicator of the ability of MM to drive *Hydra* contraction
273 than rotor unidirectionality. Further experiments are needed to elucidate both the biological
274 machinery responsible for amplifying MM-induced signals and the factors influencing MM
275 propensity for causing ICW in *Hydra* (see the discussion in the Supplemental Information).

276 The contractile behavior of *Hydra* in relation to the presentation of stimulus is detailed in
277 Supplementary Figs. 18-22. *Hydra* appeared to exhibit a photic response to light in the absence of
278 MM (Supplementary Fig. 22; $P = 0.0525 > 0.05$) consistent with the photosensitivity of the
279 hypostome and tentacles described previously[43]. However, fast-rotating MM actuation was notably
280 superior at driving muscle contraction compared to light alone. Peak identification algorithms were
281 employed to track calcium spikes in the fluorescence data and contraction bursts across the
282 timescale of our experiments. In *Hydra* treated with MM **2** and light, contraction onset occurs
283 predominantly upon the presentation of the stimulus, and a high density of contraction bursts
284 appears 5-10 seconds later (Supplementary Fig. 19). In the absence of MM, this relationship
285 weakens dramatically. In the absence of light, it disappears completely (Supplementary Fig. 22).
286 These results suggest that the actuation of fast-rotating MM can control the behaviors exhibited by
287 *Hydra* over the time scale of our experiments.

288

289 **Conclusion**

290 This work demonstrated that the activation of MM triggers calcium waves in a fashion that
291 depends on their fast, unidirectional rotation. MM localized to the endoplasmic reticulum, where
292 their activation with sub-second pulses of visible light caused a rapid rise in intracellular calcium

293 that propagated to neighboring cells. These ICW were shown to arise from $IP_3$ signaling. The
294 amplitude of MM-induced ICW was tunable by the laser light intensity. MM-induced ICW
295 remotely triggered muscle contraction *in vitro* and *in vivo*, suggesting that MM can be used for
296 molecular-scale mechanical control of biological activity.
297
298

299 **Experimental Methods.**

300 *Synthetic Chemistry*

301 Details on the synthesis and characterization of MM **2-4** are provided in the Supplementary
302 Information (Materials & Methods; Supplementary Figs. 23-28). Synthesis and characterization
303 information on MM **1** is provided elsewhere[28]. MM were dissolved in DMSO at a concentration
304 of 8 mM and sonicated for 5 s prior to use. MM solutions were stored at -20 ºC in aluminum foil-
305 wrapped containers to avoid degradation. UV-Vis spectra of MM were taken in spectral-grade
306 water using a Shimadzu UV-3600 Plus spectrophotometer. Extinction coefficients were calculated
307 by constructing a Beer's Law plot using concentrations between 8 and 32 µM.

308

309 *Cell Culture and Preparation of Cells for Microscopy*

310 HEK293 cells were chosen as the principal model system due to their widespread use in
311 electrophysiological studies. HEK cells, like most excitable or non-excitable cells, are known to
312 exhibit calcium responses[44]. HEK293 cells, HeLa cells, and N2A cells were cultured in DMEM
313 (Lonza) supplemented with 10% FBS (Gibco), and 1% penicillin/streptomycin (Lonza) at 37 ºC
314 in 5% $CO_2$ atmospheric conditions. Cells were passaged at <90% confluence. To grow
315 cardiomyocytes, a dissolved rat heart (TransnetYX©) was triturated, centrifuged, and resuspended
316 in cardiomyocyte growth medium (TransnetYX© catalog #SKU-NBCG) and seeded at a
317 concentration of 60,000 cells $cm^{-2}$. Growth substrates were pre-treated with 1% gelatin solution
318 for 3 h, then washed with PBS. Cardiomyocytes were allowed to grow for 4 days, after which the
319 growth medium was exchanged for cardiomyocyte maintenance medium (TransnetYX© catalog
320 #SKU-NBCM). Experiments were conducted from day 4 to day 6.

321 Imaging was performed in imaging extracellular buffer (iECB; 119 mM NaCl, 5 mM KCl,
322 10 mM HEPES, 2 mM $CaCl_2$, 1 mM $MgCl_2$ (pH 7.2); 320 mOsm). Cells were prepared for
323 imaging by seeding a 35 mm Ibidi imaging dish with ~50,000 cells in 1 mL of complete growth
324 medium, and grown for 2 days. Prior to imaging, cells were incubated with dyes and/or molecules
325 resuspended in complete growth medium at the appropriate concentration [MM **1** (8 μM), MM **2**
326 (8 μM), MM **3** (24 μM), MM **4** (8 μM), Fluo-4 (2 μM)]. MM and Fluo-4 were incubated with cells
327 for 45 min. Unless otherwise specified, all experiments were performed in triplicate.
328
329 *In vitro Imaging and Stimulation*
330 Cells were imaged with a Nikon A1-Rsi confocal system mounted on a widefield Ti-E
331 fluorescence microscope. Imaging was performed using a 60x water immersion objective (NA of
332 1.27, 0.17 mm working distance). Green fluorophores (Fluo-4, MitoTracker Green) were excited
333 with a 488 nm photodiode laser. Red fluorophores (ER-Tracker-Red, PI) were excited with a 561
334 nm photodiode laser. Deep red fluorophores (CellMask plasma membrane stain) were excited with
335 a 630 nm photodiode laser. Laser stimulation for *in vitro* experiments was performed with a 400
336 nm photodiode laser (Coherent OBIS™ LX SF) operating in a fluorescence-recovery-after-
337 photobleaching (FRAP) experiment mode, delivering up to $6.4\times10^2$ W $cm^{-2}$ at sample level. *In*
338 *vitro* experiments with HEK293 cells were conducted using a stimulus irradiance of $3.2\times10^2$ W
339 $cm^{-2}$ except where otherwise indicated. Cardiomyocyte experiments were conducted using a
340 stimulus irradiance of $5.1\times10^2$ W $cm^{-2}$. Power was calibrated using a Thor Labs S130C laser power
341 meter. Stimulation was targeted to a circular area of diameter 5 μm in a 250 ms pulse, during which
342 the laser rastered across the entire region of interest. An additional laser stimulation set-up was
343 used to verify the requisite stimulation power and demonstrate excitation in a non-scanning laser

344 mode (see Supplementary Fig. 29 and the accompanying discussion). Fluo-4 fluorescence was
345 collected for ~30 s before and 2 min after stimulation (since the recorded time of the first data
346 point is 0 s, stimulation occurs between 28.6 and 28.85 s in recorded traces). Images were collected
347 using a Galvano scanner operating at 0.94 fps. In some experiments, images were also collected
348 using a resonant scanner operating at 7.7 fps.
349
350 *Colocalization Analysis*
351 Cells were treated with MitoTracker Green (ThermoFisher, 400 nM), ER Tracker Red
352 (ThermoFisher, 500 nM), and CellMask Deep Red Plasma Membrane Stain (ThermoFisher, 500
353 nM). ER Tracker Red and MitoTracker Green were loaded into cells for 45 min in complete growth
354 medium. Then, CellMask Deep Red Plasma Membrane Stain was loaded into cells for 5 min and
355 cells were subsequently loaded into the microscope chamber. Images for co-localization analysis
356 were collected in a Nikon A1 confocal microscope using a 60x water immersion objective. Z-stack
357 images spanning a minimum 20 µm range were collected and processed using the Coloc-2 plugin
358 in Fiji. Colocalized pixel intensity maps were generated using the colocalization threshold function
359 in Fiji.
360
361 *Pharmacological Experiments.*
362 In pharmacological blocking experiments, cells were loaded with MM and Fluo-4 as
363 previously described. Typical imaging experiments were then performed on six cells in iECB alone
364 as a positive control. Then, the imaging buffer was replaced, and the cells were treated as required
365 for each experiment (see below). After a brief recovery period, six non-previously imaged cells
366 were stimulated and imaged. Phosphate-buffered saline (PBS) was used for experiments in

367 calcium-free buffer. Thapsigargin (Th; 1 μM) and cytochalasin D (Cyto D; 2 μM) were incubated
368 with cells in the incubator in complete growth medium for 1 h (Th) or 2 h (Cyto D) before imaging.
369 Ruthenium red (RR; 1 μM), gadolinium ($Gd^{3+}$; 50 μM), ryanodine (Ry; 100 μM), xestospongin C
370 (XeC; 20 μM), and U-73122 (U-73; 10 μM) were administered directly into the iECB after control
371 imaging was finished. Cells were incubated in the medium for ~5 min prior to imaging. For
372 experiments using ROS scavengers, cells were incubated with either melatonin (Mel; 100 μM),
373 thiourea (thioU; 50 mM), or L-ascorbic acid (VitC; 2 mM) for 1 h prior to experiments. The traces
374 shown are representative results across at least six cells from individual experiments, while bar
375 graphs represent the average results across at least three distinct experiments. See Supplementary
376 Table 2 for more information.
377
378 *Hydra Preparation*
379 *Hydra* were grown in *Hydra* medium containing $CaCl_2 \cdot 2H_2O$ (1 mM), $MgCl_2 \cdot 6H_2O$ (0.1
380 mM), $KNO_3$ (0.03 mM), $NaHCO_3$ (0.5 mM), and $MgSO_4$ (0.08 mM) in deionized water at 18 $^oC$
381 in a light-cycled (12 h light, 12 h dark) incubator. *Hydra* were fed with an excess of freshly brined
382 *Artemia Nauplii* (Brine Shrimp Direct, Ogden, UT, # BSEP 8Z) three times a week. All
383 experiments were performed at room temperature after starving the animals for 2 days. The
384 transgenic line expressing calcium indicator GCaMP7b under the Ef1α promoter in endodermal
385 epitheliomuscular tissue was generated by embryonic microinjection in a collaboration by the
386 Robinson lab (Rice University) and the Juliano lab (University of California, Davis)[42].
387
388 *Hydra Imaging and Stimulation*

389 *Hydra* were incubated with the selected MM for 24 h before imaging. Stimuli were applied
390 using an ROI-driven fluorescence-recovery-after-photobleaching (FRAP) mode in a Nikon A1
391 confocal microscope. All *Hydra* were able to recover after stimulation experiments, indicating
392 both MM administration and subsequent stimulation treatments were not toxic to the *Hydra*.
393 Distinct stimulation protocols were employed to elicit either regional ICW or whole-body
394 contraction. In Protocol **I**, stimulation was delivered using a 405-nm laser diode at $9.0\times10^2$ W $cm^{-}$
395 $^{2}$ in 1 s pulses delivered to a 10 μm region of the *Hydra* body column. Protocol **I** resulted in regional
396 ICW. In Protocol **II**, stimulation was delivered using a 405-nm laser diode at $9.0\times10^2$ W $cm^{-2}$ in
397 a 2 s pulse delivered to the oral region of the *Hydra* (typical area of ~1,000-2,000 $\mu m^2$). Protocol
398 **II** resulted in whole-body calcium waves and contraction. Note that despite the longer stimulation
399 time used in Protocol **II**, the *Hydra* still experiences less pixel dwell time and less incident light
400 per unit area compared to *in vitro* experiments and Protocol **I** due to the size of the stimulation
401 region (~50-100x larger depending on the size of the animal). GCaMP7b fluorescence were
402 recorded using a 456 nm laser diode for fluorophore excitation. In experiments using Protocol **I**,
403 stimuli were presented at 10 s. In experiments using Protocol **II**, stimuli were presented at irregular
404 intervals at least 60 s apart to prevent interference from periodic spontaneous contractions of
405 *Hydra*.
406
407 *Data Analysis*
408 Data were analyzed using custom-written Python scripts. Fluorescence traces of the
409 calcium indicator Fluo-4 from cells were imported and processed using the Pandas library. $F_0$ was
410 calculated as the average fluorescence intensity in the first 10 frames (~10 s) of the acquisition and
411 used to calculate $\Delta F/F_0$ over the entire length of the acquisition. Since data was not collected

412 during stimulation, a “dead time” equivalent to the time of stimulation was manually added to each
413 recording. Spiking behavior of cardiomyocytes was calculated using the SciPy peak finder
414 function.

415 Fluorescence traces of calcium indicator GCaMP7b in *Hydra vulgaris* were processed
416 similarly to *in vitro* data and baseline-corrected to set the minimum measured $\Delta F/F_0$ value as “0”
417 due to the spontaneous, periodic activity of the *Hydra*. For experiments analyzing regional ICW
418 (stimulating using Protocol **I**), responses reaching $\Delta F/F_0 > 1$ in the stimulated area were
419 considered a “success” in the calculation of the ICW response rate. The “delay time” was the time
420 at which $\Delta F/F_0$ reached 1. Peaks corresponding to whole-body contraction were not included in
421 the analysis of ICW amplitude. ICW response rate was calculated across n=25 experiments for
422 each condition across at least 5 *Hydra*.

423 In experiments analyzing whole-body contraction (stimulating using Protocol **II**), the
424 induction of a contractile “response” comprising a change in body GCaMP7b fluorescence of
425 $\Delta F/F_0 > 1.5$x within 3 s of stimulus presentation was counted as a “success” in the calculation of
426 the contractile response rate. To identify contraction onset, a limit-of-detection peak finding
427 algorithm was used with a threshold value of 1.5. To identify individual calcium spikes in a
428 contraction burst, the SciPy peak finder function was employed. Induction of a contractile
429 "response" comprising a change in body GCaMP7b fluorescence of $\Delta F/F_0 > 1.5$x within 3 s of
430 stimulus presentation was considered a "success" when calculating response rates. Response rates
431 were calculated over at least 50 presentations of stimuli. Stimuli presented at a time when the
432 *Hydra* were already contracting ($\Delta F/F_0 > 0.3$) were discarded. *Hydra* that exhibited mouth-
433 opening behavior during the experiment were discarded. The effects of spontaneous and photic

434 responses were accounted for by comparison with DMSO and DMSO and light controls. For more
435 information on *Hydra* data processing, see Supplementary Table 3.
436
437 *Statistical Analysis*
438 One-tailed Welch's t-tests were performed to assess differences in cellular responses after
439 pharmacological manipulations, or when treated with MM of different rotation speeds. Fisher's
440 Exact Tests was used to assess differences in contractile response rates between *Hydra vulgaris*
441 treated with MM of variable rotation speed and light. * $P$-value < 0.05, ** $P$-value < 0.01, ***
442 $P$-value < 0.001, **** $P$-value < 0.0001.
443
444 **Acknowledgements**.
445 This project received funding from the Discovery Institute, the Robert A. Welch
446 Foundation (C-2017-20190330), the National Science Foundation Graduate Research Fellowship
447 Program (JLB), the DEVCOM Army Research Laboratory under Cooperative Agreement
448 W911NF-18-2-0234 (AVV), and the European Union's Horizon 2020 research and innovation
449 programme under the Marie Skłodowska-Curie grant agreement No. 843116 (ALS). The views
450 and conclusions contained in this document are those of the authors and should not be interpreted
451 as representing the official policies, either expressed or implied, of the Army Research Laboratory
452 or the U.S. Government. The U.S. Government is authorized to reproduce and distribute reprints
453 for Government purposes notwithstanding any copyright notation herein. The funders had no role
454 in the study design, data collection and analysis, decision to publish, or preparation of the
455 manuscript. This work was conducted in part using resources from the Light Microscopy Facility
456 and the Shared Equipment Authority at Rice University. The authors acknowledge Zachary C.

Sanchez (Vanderbilt University) for useful help and advice regarding growth and activity of cardiomyocytes.

**Author Contributions.**

Conceptualization, JLB, ARV, JMT.

Methodology, JLB, GD, SK, JZ, ALS.

Organic synthesis: ARV, GL, BL, JMT.

Formal analysis, JLB.

Investigation, JLB, SK, GC, DA, JZ.

Resources, JTR, JMT.

Writing, Original draft, JLB.

Writing, Reviewing, and Editing, JLB, GD, SK, ALS, JTR, JMT.

Visualization, JLB.

Supervision, GD, JTR, JMT.

Funding acquisition, JMT.

Project oversight: JMT.

**Declaration of interests**

Rice University owns intellectual property on the use of electromagnetic (light) activation of MM for the stimulation of intercellular calcium waves. Conflicts of interest are managed through regular disclosure to the Rice University Office of Sponsored Projects and Research Compliance. The authors declare no other competing interests.

**Biological materials**

480 All biological materials used in this work are available from commercial sources.

481 **Data availability**

482 All data supporting the findings of this study are available within the article and its supplementary
483 information files.

484 **Code availability.**

485 Data analysis scripts are available upon request to the author, JMT.

486

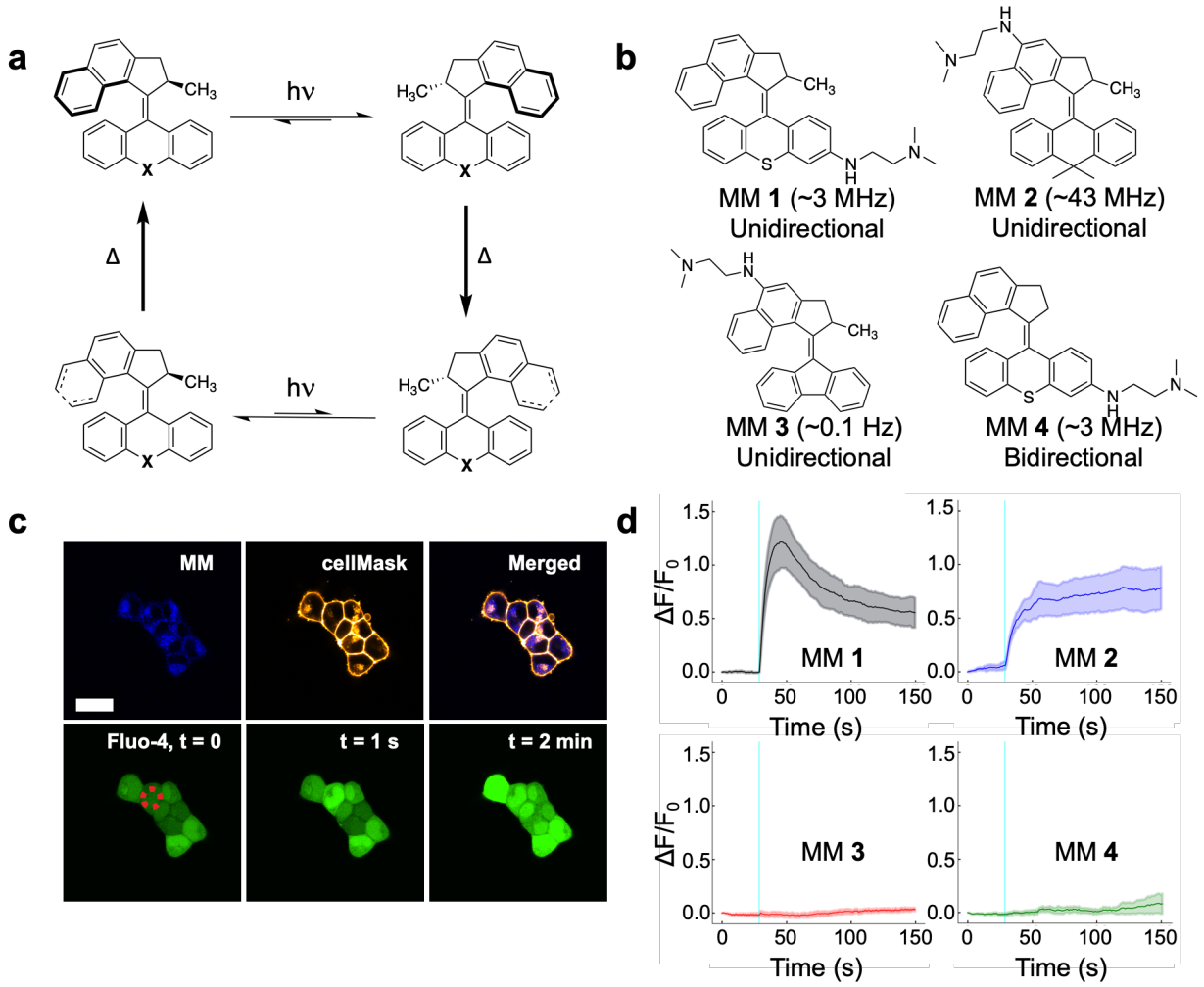


**Fig. 1. Structures of MM used in this study, their mechanism of rotation, and their activation to induce ICW in HEK293 cells. (a)** The rotation cycle of a typical MM, showing two photoisomerizations (hν) and two thermal (Δ) helix inversions to complete a unidirectional rotation. The moiety in the "X" position can be changed to synthesize MM of different rotation speeds. **(b)** Structures of the MM employed in this study. MM **1** and MM **2** complete fast (MHz-scale) unidirectional rotation. MM **3** rotates at 0.1 Hz at room temperature. MM **4** lacks chirality imparted by the allylic methyl and possesses no preference for unidirectional rotation. **(c)** Confocal microscope images of cells treated with MM **1**, calcium-tracking dye Fluo-4, and cell membrane labeling dye CellMask (used to differentiate individual cells), showing a rapid increase in

497 intracellular calcium levels after stimulation with 400 nm light. The red dotted circle labels the
498 area of laser stimulation. The images in the top row were taken before stimulation, and the images
499 in the bottom row were taken immediately prior to, 1 s after, and 2 min after stimulation. The scale
500 bar applies to all images and is 20 μm. **(d)** Representative normalized fluorescence intensity traces
501 of Fluo-4 in HEK293 cells treated with each MM. The solid line represents the average responses
502 of n=6 independent cells, and the shaded area represents the standard error of the mean. MM **1**,
503 MM **2**, and MM **4** were administered to cells at 8 μM. MM **3** was administered to cells at 24 μM.
504 Stimuli for cells treated with MM **1**, **2**, and **4** used a 250 ms pulse width delivered to a circular area
505 of diameter 5 μm at $3.2\times10^{2}$ W $cm^{-2}$. Stimuli for cells treated with MM **3** were administered at
506 $6.4\times10^{2}$ W $cm^{-2}$. For all plots, the cyan line indicates the time of stimulus presentation.
507

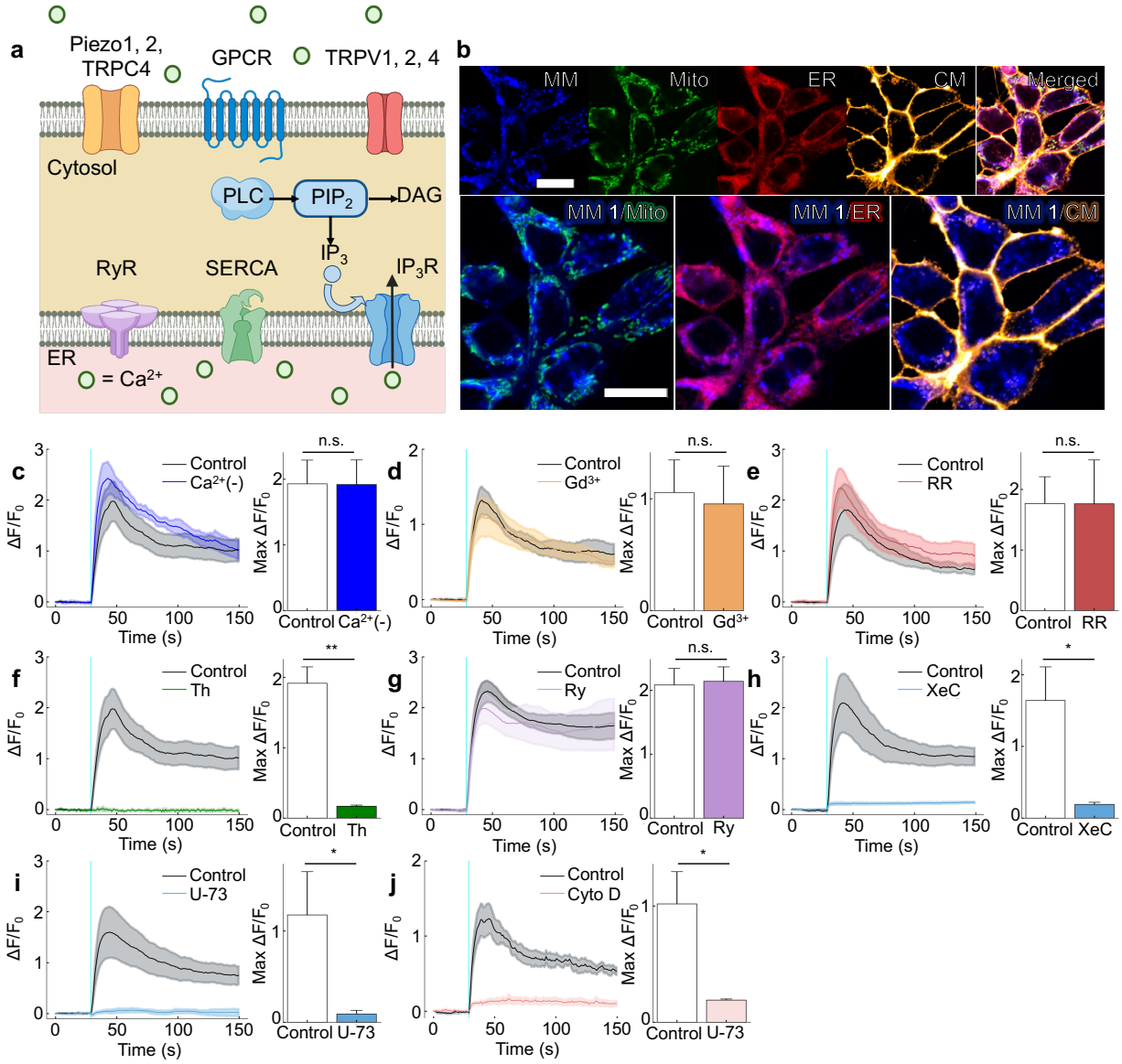


**Fig. 2. Mechanistic study of MM-induced ICW. (a)** Schematic of possible mechanisms by which calcium can enter the cytoplasm. Prepared with Biorender.com. **(b)** Confocal microscope images of HEK293 cells treated with MM **1**, MitoTracker Green, ER Tracker Red, and CellMask Deep Red. Scale bars are both 20 μm and apply to the images in the same row. **(c-h)** Calcium waves elicited by MM **1**-treated cells **(c)** in calcium-free PBS, **(d)** in RR (1 μM), **(e)** in $Gd^{3+}$ (50 μM), **(f)** after treatment of cells with Th (1 μM), **(g)** in Ry (100 μM), **(h)** in XeC (25 μM), **(i)** in U-73 (10 μM), **(j)** after pre-treatment of cells with Cyto D (2 μM). The solid line represents the calcium

516 profiles averaged from six independent cells. The shaded region represents the standard error of
517 the mean (n=6). Stimuli were presented after 30 s of imaging in each case, and the time of stimulus
518 presentation is indicated by the vertical cyan line. For all plots, the black trace shows a positive
519 control consisting of MM **1**-treated cells in typical imaging buffer recorded on the same day. All
520 stimuli were delivered with a pulse width of 250 ms to a circular area of diameter 5 μm at a power
521 ranging from $3.2\times10^{2}$ W $cm^{-2}$ to $5.1\times10^{2}$ W $cm^{-2}$. For all plots, the cyan line indicates the time of
522 stimulus presentation. Controls and experimental groups were imaged and stimulated on the same
523 day using the same conditions and with the same batch of cells. Error bars in the bar graphs
524 represent the standard deviation of the mean of n=3 experiments (at least 6 stimulated cells per
525 experiment). Statistical analyses were performed using a one-tailed Welch's t-test. * *P*-value <
526 0.05, ** *P*-value < 0.01, *** *P*-value < 0.001, **** *P*-value < 0.0001.
527

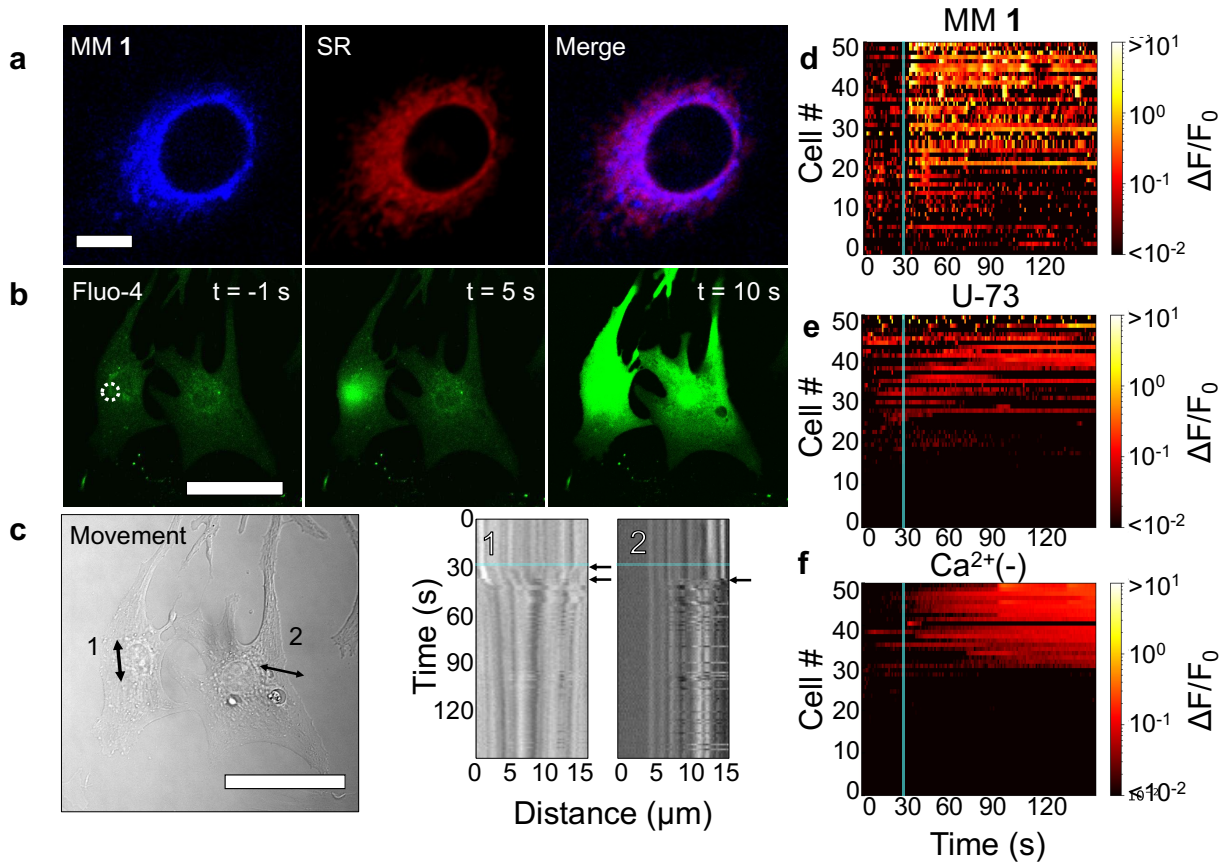


528

529 **Fig. 3. MM-induced calcium waves cause localized calcium release, contraction, and beating**
530 **in cardiomyocytes. (a)** Confocal microscope images of a single myocyte treated with MM **1** and
531 ER Tracker Red. The scale bar is 10 μm and applies to all images. **(b)** Confocal microscope images
532 showing Fluo-4 fluorescence, revealing calcium activity in cardiomyocytes before and after
533 stimulation. The scale bar is 50 μm and applies to all images. The white circle represents the
534 stimulation region. **(c)** Kymographs representative of cardiac myocyte contractile responses from
535 the same cells shown in (b). The line profiles from which kymographs **1** and **2** were taken are
536 shown as double-sided arrows in the bright field image. Kymographs **1** and **2** were taken from the
537 stimulated cell and an adjacent cell, respectively. The scale bar in the bright field image is 50 μm.
538 Kymograph **1** shows local contraction in the stimulated cell (top arrow in **1**), indicated by a
539 convergence of the edges in the kymograph plot. Both kymographs **1** and **2** show periodic beating

540 in the stimulated cell and surrounding cell (bottom arrow in **1** and arrow in **2**). **(d-f)** Normalized
541 fluorescence intensity change of Fluo-4 in cardiomyocytes adjacent to stimulated cardiomyocytes
542 that were treated with **(d)** MM **1** alone, **(e)** MM **1** and U-73 (10 μM), and **(f)** MM **1** in calcium-
543 free PBS. For each condition, n=50 cells were used. The x-axis label in (f) also applies to (d-e).
544 All stimulation experiments were performed with a stimulation time of 250 ms at $5.1\times10^{2}$ W $cm^{-2}$
545 in a circular region of 5 μm diameter using a 400 nm laser. In all plots, the cyan line indicates the
546 time of stimulus presentation.
547

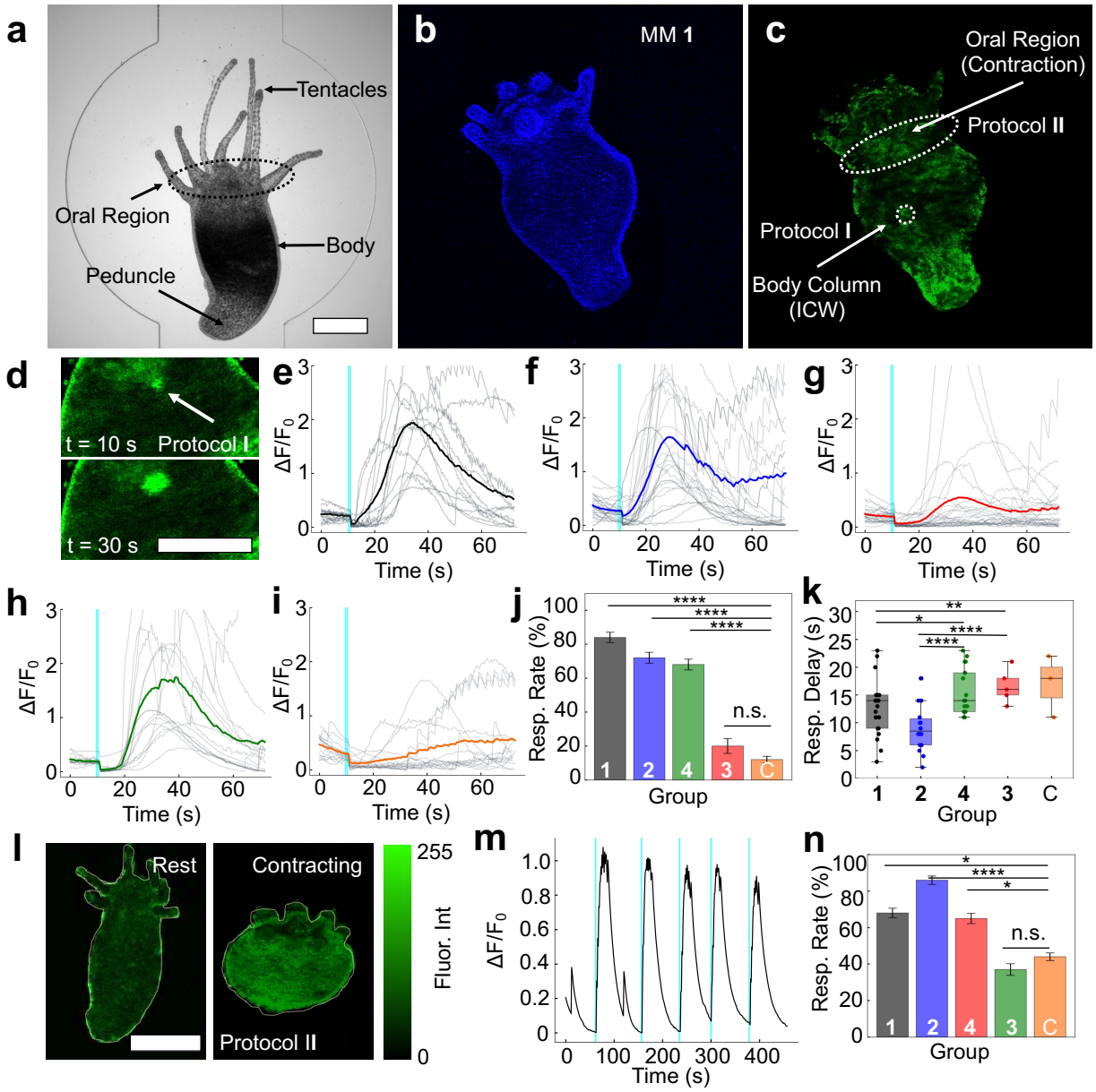


548

549 **Fig. 4. MM induce ICW and muscle contraction *in vivo*. (a)** Image of a *Hydra* loaded into a

550 microfluidic chamber with anatomical regions marked. Scale bar is 100 µm and applies to (a-c).

551 **(b)** MM **1** (24 µM) loaded into *Hydra* for 24 h. **(c)** A *Hydra* expressing GCaMP7b in

552 endodermal epitheliomuscular cells. The stimulation regions used for Protocols **I** and **II** are

553 marked. Protocol **I** was used for body column stimulation (1 s pulse to a 10 µm diameter circular

554 area) to trigger regional ICW. Protocol **II** was used for oral region stimulation (2 s pulse to the

555 oral region, ~1000-2000 μm$^2$) to trigger whole-body contraction. **(d)** A regional ICW in a *Hydra*
556 treated with MM **1** and stimulated with 405-nm light via Protocol **I**. The indicated times
557 represent the time after stimulation at which the image was taken. Scale bar applies to both
558 images and is 100 μm. **(e-i)** Responses observed from *Hydra* treated with **(e)** MM **1**, **(f)** MM **2**,
559 **(g)** MM **3**, **(h)** MM **4**, or **(i)** DMSO control ("C") and stimulated for 1 s using Protocol **I**. Bold,
560 colored traces represent the average trace (n=25 across 5 *Hydra*). Gray traces represent
561 individual experiments. **(j)** Bar graph showing ICW response rate and **(k)** box-and-whisker plot
562 showing ICW delay time of *Hydra* stimulated using Protocol **I** across MM treatment conditions
563 (n=25 experiments across at least 5 *Hydra* per condition). ICW responses were defined as $\Delta F/F_0$
564 > 1. **(l)** Representative contraction in a *Hydra* treated with MM **2** and stimulated via Protocol **II**.
565 Scale bar applies to both images and is 100 μm. **(m)** Representative GCaMP7b fluorescence
566 trace in a *Hydra* treated with MM **2** and stimulated using Protocol **II**. **(n)** Bar graph showing
567 contractile response rates across treatment conditions for *Hydra* stimulated for 2 s using Protocol
568 **II** (at least 50 experiments across ≥5 *Hydra* per condition). Error bars in bar graphs represent the
569 standard error of the mean. See *Methods* for more info on the calculation of ICW and contractile
570 response rates. For all plots, cyan lines indicate the time of stimulus with 405-nm light ($9.0\times10^2$
571 W cm$^{-2}$), during which no data was collected. * *P*-value < 0.05, ** *P*-value < 0.01, *** *P*-value <
572 0.001, **** *P*-value < 0.0001.

573 **References.**


574 1. Clapham, D. E. Calcium Signaling. *Cell* **131**, 1047–1058 (2007).

575 2. Tsutsumi, M. *et al.* Mechanical-stimulation-evoked calcium waves in proliferating and
576 differentiated human keratinocytes. *Cell Tissue Res.* **338**, 99–106 (2009).

577 3. Screaton, R. A. *et al.* The CREB Coactivator TORC2 Functions as a Calcium- and cAMP-
578 Sensitive Coincidence Detector. *Cell* **119**, 61–74 (2004).

579 4. Carrasco, M. A. & Hidalgo, C. Calcium microdomains and gene expression in neurons and
580 skeletal muscle cells. *Cell Calcium* **40**, 575–583 (2006).

581 5. Glaser, T. *et al.* ATP and spontaneous calcium oscillations control neural stem cell fate
582 determination in Huntington's disease: a novel approach for cell clock research. *Mol. Psychiatry*
583 **26**, 2633–2650 (2021).

584 6. Tada, M. & Concha, M. L. Vertebrate gastrulation: Calcium waves orchestrate cell
585 movements. *Curr. Biol.,* **11**, R470–R472 (2001).

586 7. McCormack, J. G., Halestrap, A. P., & Denton, R. M. Role of calcium ions in regulation
587 of mammalian intramitochondrial metabolism. *Phys. Rev.,* **70**, 391-425 (1990).

588 8. Leybaert, L. & Sanderson, M. J. Intercellular $Ca^{2+}$ Waves: Mechanisms and Function.
589 *Phys. Rev.* **92**, 1359–1392 (2012).

590 9. G., Eng, *et al*., Autonomous beating rate adaptation in human stem cell-derived
591 cardiomyocytes. *Nat Commun* **7**, 10312 (2016).

592 10. Llano, I. *et al.,* Presynaptic calcium stores underlie large-amplitude miniature IPSCs and
593 spontaneous calcium transients. *Nat Neurosci* **3**, 1256–1265 (2000).

594 11. Takano, T. *et al.,* Astrocyte-mediated control of cerebral blood flow. *Nat Neurosci* **9**, 260–
595 267 (2006).

596 12. Drumm, B. T. *et al.,* The effects of mitochondrial inhibitors on Ca2+ signalling and
597 electrical conductances required for pacemaking in interstitial cells of Cajal in the mouse small
598 intestine. *Cell Calcium* **72**, 1–17 (2018).
599 13. Gourine, A. V. *et al.,* Astrocytes Control Breathing Through pH-Dependent Release of
600 ATP. *Science* **329**, 571–575 (2010).
601 14. Berridge, M. J. Calcium signaling remodeling and disease. *Biochem. Soc. Trans.,* **40,** 297-
602 309 (2012).
603 15. Stewart, T. A., Yapa, K. T. D. S., & Monteith, G. R. Altered calcium signaling in cancer
604 cells. *Biochim Biophys Acta Biomembr.,* **1848,** 2502-2511 (2015).
605 16. Berridge, M. J., Lipp, P., Bootman, M. D. The versatility and universality of calcium
606 signaling. *Nat. Rev. Molec. Cell Biol.,* **1,** 11-21 (2000).
607 17. Cornell-Bell, A. H. *et al.,* Glutamate Induces Calcium Waves in Cultured Astrocytes:
608 Long-Range Glial Signaling. *Science* **247**, 470–473 (1990).
609 18. Sanderson, M. J., Charles, A. C. & Dirksen, E. R. Mechanical stimulation and intercellular
610 communication increases intracellular $Ca^{2+}$ in epithelial cells. *Cell Regul* **1**, 585–596 (1990).
611 19. Klok, M. *et al.* MHz Unidirectional Rotation of Molecular Rotary Motors. *J. Am. Chem.*
612 *Soc.* **130**, 10484–10485 (2008).
613 20. García-López, V. *et al.* Unimolecular Submersible Nanomachines. Synthesis, Actuation,
614 and Monitoring. *Nano Lett.,* **15,** 8229-8239 (2015).
615 21. García-López, V. *et al.* Molecular machines open cell membranes. *Nature* **548**, 567–572
616 (2017).
617 22. Zheng, Y. *et al.* Optoregulated force application to cellular receptors using molecular
618 motors. *Nat. Commun.,* **12**, 3580 (2021).

619 23. García-López, V., Liu, D., & Tour, J. M. Light-activated organic molecular motors and
620 their applications. *Chem. Rev.,* **120,** 79-124 (2020).
621 24. Pollard, M. M., Klok, M., Pijper, D. & Feringa, B. L. Rate Acceleration of Light-Driven
622 Rotary Molecular Motors. *Adv. Func. Mater.,* **17**, 718–729 (2007).
623 25. Kepp, O., Galluzzi, L., Lipinski, M., Yuan, J. & Kroemer, G. Cell death assays for drug
624 discovery. *Nat Rev Drug Discov*., **10**, 221–237 (2011).
625 26. Galbadage, T. *et al.* Molecular nanomachines disrupt bacterial cell wall, Increasing
626 sensitivity of extensively drug-resistant *Klebsiella pneumoniae* to meropenem. *ACS Nano* **13**,
627 14377–14387 (2019).
628 27. Santos, A. L. *et al.* Light-activated molecular machines are fast-acting broad-spectrum
629 antibacterials that target the membrane. *Sci. Adv.,* **8**, eabm2055 (2022).
630 28. Alaya-Orozco, C. *et al.* Visible-light-activated molecular nanomachines kill pancreatic
631 cancer cells. *ACS Appl. Mater. Int.,* **12,** 410-417 (2020).
632 29. Vriens, J. ,Appendino, G., & Nilius, B. Pharmacology of vanilloid transient receptor
633 potential cation channels. *Mol. Pharmacol.,* **75,** 1262-1279 (2009).
634 30. Hamill, O. P. & McBride Jr., D. W. The pharmacology of mechanogated membrane ion
635 channels. *Pharmacol. Rev.,* **48,** 231-252 (1996).
636 31. Thastrup, O., Cullen, P. J., Drøbak, B. K., Hanley, M. R. & Dawson, A. P. Thapsigargin,
637 a tumor promoter, discharges intracellular $Ca^{2+}$ stores by specific inhibition of the endoplasmic
638 reticulum $Ca^{2+}$-ATPase. *PNAS* **87**, 2466–2470 (1990).
639 32. Bock, G. R. & Ackrill, K. *Calcium Waves, Gradients and Oscillations*. (John Wiley &
640 Sons, 2008).

641 33. Gafni, J. *et al.* Xestospongins: potent membrane permeable blockers of the inositol 1,4,5-
642 trisphosphate receptor. *Neuron,* **19,** 723-733 (1997).
643 34. Ribeiro, C. M. P., Reece, J. & Putney, J. W. Role of the Cytoskeleton in Calcium Signaling
644 in NIH 3T3 Cells. *J. Biol. Chem.,* **272**, 26555–26561 (1997).
645 35. Xu, J. *et al.* GPR68 senses flow and is essential for vascular physiology. *Cell,* **173**, 762-
646 775.e16 (2018).
647 36. Feher, J. *Quantitative Human Physiology: An Introduction*. (Elsevier, 2007).
648 37. Stuyvers, B. D., Boyden, P. A. & ter Keurs, H. E. D. J. Calcium waves. *Circ. Res.,* **86**,
649 1016–1018 (2000).
650 38. Wang, H. *et al.* From neuron to muscle to movement: a complete biomechanical model of
651 *Hydra* contractile behaviors. *bioRxiv* (2020). doi:10.1101/2020.12.14.422784.
652 39. Kinnamon, J. C. & Westfall, J. A. A three dimensional serial reconstruction of neuronal
653 distributions in the hypostome of a *Hydra*. *J. Morphol.,* **168**, 321–329 (1981).
654 40. Kinnamon, J. C. & Westfall, J. A. Types of neurons and synaptic connections at
655 hypostome-tentacle junctions in *Hydra*. *J. Morphol.,* **173**, 119–128 (1982).
656 41. Dupre, C. & Yuste, R. Non-overlapping neural networks in *Hydra* vulgaris. *Curr. Biol.,*
657 **27**, 1085–1097 (2017).
658 42. Badhiwala, K. N., Primack, A. S., Juliano, C. E., & Robinson, J. T. Multiple neuronal
659 networks coordinate *Hydra* mechanosensory behavior. *eLife*, 10:e64108 (2020).
660 43. Guertin, S. & Kass-Simon, G. Extraocular spectral photosensitivity in the tentacles of
661 *Hydra* vulgaris. *Comp. Biochem. Physiol. Part A Mol. Integr. Physiol.* **184**, 163–170 (2015).

662 44. Sinnecker, D. & Schaefer, M. Real-time analysis of phospholipase C activity during
663 different patterns of receptor-induced $Ca^{2+}$ responses in HEK293 cells. *Cell Calcium* **35**, 29–38
664 (2004).
665 45. Roke, D. *et al.* Light-gated rotation in a molecular motor functionalized with a
666 dithienylethene switch. *Angew. Chem., Int. Ed.*, **57**, 10515–10519 (2018).
667 46. Saywell, A. *et al.* Light-induced translation of motorized molecules on a surface. *ACS Nano*
668 **10**, 10945–10952 (2016).
669 47. Zhao, X., Fan, B., Hassan, S., Veeraraghavan, A., & Robinson, J. T. Near field optical
670 sensing of single cell activity with integrated micro-ring resonators. *Biophotonics Congress 2021,*
671 OSA Technical Digest (Optical Society of America, 2021), paper BTu3B.4.
672 48. Gunasekera, R. S. *et al.* Molecular nanomachines can destroy tissue or kill multicellular
673 eukaryotes. *ACS Appl. Mater. Int.,* **12,** 13657-13670 (2020).
674 49. Hajnoczky, G., Davies, E., & Madesh, M. Calcium signaling and apoptosis. *Biochem.*
675 *Biophys. Ref. Commun.,* **304,** 445-454 (2003).
676 50. Cnossen, A., Kistemaker, J. C. M., Kojima, T., & Feringa, B. L. Structural dynamics of
677 overcrowded alkene-based molecular motors during thermal isomerization. *J. Org. Chem.,* **79,**
678 927-935 (2014).
679 51. Grigoryan, B. *et al.* Development, characterization, and applications of multi-material
680 stereolithography bioprinting. *Sci. Rep.*, **11**, 3171 (2021).